Orientation and Stability of Asymmetric Magnetic Reconnection X Line

Yi-Hsin Liu[1], **M. Hesse**[2,3], **T.C. Li**[1], **M. Kuznetsova**[4], and **A. Le**[5]

[1]Department of Physics and Astronomy, Dartmouth College, Hanover, NH, USA

[2]Department of Physics and Technology, University of Bergen, Bergen, Norway

[3]Southwest Research Institute, San Antonio, TX, USA

[4]NASA-Goddard Space Flight Center, Greenbelt, MD, USA

[5]Los Alamos National Laboratory, Los Alamos, NM, USA

Abstract

The orientation and stability of the reconnection x line in asymmetric geometry is studied using three-dimensional (3-D) particle-in-cell simulations. We initiate reconnection at the center of a large simulation domain to minimize the boundary effect. The resulting x line has sufficient freedom to develop along an optimal orientation, and it remains laminar. Companion 2-D simulations indicate that this x line orientation maximizes the reconnection rate. The divergence of the nongyrotropic pressure tensor breaks the frozen-in condition, consistent with its 2-D counterpart. We then design 3-D simulations with one dimension being short to fix the x line orientation but long enough to allow the growth of the fastest growing oblique tearing modes. This numerical experiment suggests that reconnection tends to radiate secondary oblique tearing modes if it is externally (globally) forced to proceed along an orientation not favored by the local physics. The development of oblique structure easily leads to turbulence inside small periodic systems.

1. Introduction

Magnetic reconnection plays the critical role in the plasma transport and magnetic energy release at Earth's magnetopause, the sharp boundary separating Earth's magnetosphere and solar wind plasmas. To understand the global convection of plasmas and magnetic flux around Earth, it is imperative to know where reconnection will take place on this boundary layer (Dungey, 1961). With purely southward interplanetary magnetic fields in the solar wind, it is clear that the dayside reconnection will occur along the equatorial plane. The resulting locus that connects these reconnection locations is called the *reconnection line* (e.g., Trattner et al., 2004). However, the location and orientation of the reconnection line become less clear when the interplanetary magnetic field points in a clock angle different than southward (i.e., the Sun-Earth direction is the rotation axis). Observations suggested a"tilted" reconnection line in this situation (Daly et al., 1984; Dunlop, Zhang, Bogdanova, Lockwood, et al., 2011; Dunlop, Zhang, Bogdanova, Trattner, et al., 2011; Fear et al., 2012;

Correspondence to: Y.-H. Liu, Yi-Hsin.Liu@Dartmouth.edu.

Kawano & Russell, 2005; Phan et al., 2006; Pu et al., 2007; Scurry et al., 1994; Trattner et al., 2007; Wild et al., 2007). A similarly tilted reconnection line was illustrated in global magnetohydrodynamics simulations by tracing the global magnetic separator (Komar et al., 2013). Predictions of the reconnection line location on the magnetopause were previously made by mapping out locations that maximize local quantities, such as the shear angle (Trattner et al., 2007), current density (Alexeev et al., 1998), and Poynting flux divergence (Papadopoulos et al., 1999). Another approach was based on the vacuum superposition of Earth dipolar and solar wind magnetic fields (Cowley, 1973; Dorelli et al., 2007; Siscoe et al., 2001).

In this work, we approach this problem from the local aspect of reconnection by studying the orientation of the reconnection x line in slab geometry. Even with this simplified geometry, understanding this 3-D nature of magnetic reconnection is already challenging and a strict theoretical treatment does not exist. Researchers have used the same principle that determines the local x line orientation to map out the reconnection location on the global magnetopause (Komar et al., 2015). The result of this study suggests that the tangent of a global reconnection line will eventually align with the local x line orientation. The question to solve and the coordinate system employed in this study are further illustrated in Figure 1. Magnetic fields on two sides of the boundary layer (like Earth's magnetopause) can shear at an arbitrary angle $. Here we consider the boundary normal to the z direction and the B_z component to be negligible. If we take a 2-D cut depicted by the black line in Figure 1a, the in-plane component of magnetic fields on the two sides are antiparallel as illustrated in Figure 1b, and thus reconnection can occur on this plane. However, this 2-D plane is not the only possible choice. We take another 2-D plane in Figure 1c, and there are also in-plane antiparallel magnetic fields for reconnection as illustrated in Figure 1d although the in-plane field strength changes on this plane. Therefore, the question to ask is, given different magnetic field and plasma conditions on two sides of the current sheet, on which plane will reconnection proceed? Since the reconnection x line (marked by the orange dashed line in Figures 1a and 1c) is always perpendicular to the corresponding 2-D reconnection plane, the goal is equivalent to determining the orientation of the x line. We will quantify the x line orientation by the angle 6 respected to the $\mathbf{y}_0$ axis (for simplicity, we choose $\mathbf{y}_0$ to be the direction where the guide field B_{y0} is uniform). Hypotheses to this well-defined question were proposed. They include minimizing the in-plane current (Gonzalez & Mozer, 1974; Sonnerup, 1974), maximizing the reconnection outflow speed (Swisdak & Drake, 2007), maximizing the reconnection rate (Aunai et al., 2016; Hesse et al., 2013; Liu et al., 2015; Schreier et al., 2010), or maximizing the oblique tearing growth rate (Liu et al., 2015). On the other hand, other than a few studies in literature (Liu et al., 2015; Schreier etal., 2010), there are not many attempts to study this fundamental nature of magnetic reconnection using first-principle 3-D simulations. To resolve the reconnection x line in the electron scale will require a fully kinetic description. Thus, we use both 3-D and 2-D particle-in-cell (PIC) simulations to explore this issue. After knowing the optimal orientation favored by the local physics, we further study the response of the system when the x line is forced to misalign with the optimal orientation. This result reveals the potential format of the interplay between the global and local controls.

The structure of this paper is outlined in the following. Section 2 describes the simulation setup. Section 3 measures the x line orientation in the large 3-D simulation. Section 4 identifies the nonideal term in Ohm's law that breaks the frozen-in condition. Section 5 shows the comparison with companion 2-D simulations and theories. Section 6 studies the response of the x line when it is forced to proceed at an orientation not favored by the local physics. Section 7 summarizes and discusses our results.

2. Simulation Setup

In this paper, kinetic simulations were performed using the electromagnetic PIC code VPIC (Bowers et al., 2009). The employed asymmetric current sheet (Aunai, Hesse, Zenitani etal., 2013; Hesse etal., 2013; Liu etal., 2015; Pritchett, 2008) has the magnetic profile, $\mathbf{B}_0 = B_0(0.5 + S)\hat{\mathbf{x}}_0 + B_0\hat{\mathbf{y}}_0$ with $S = \tanh[(z - 3d_i)/L]$, which corresponds to a shear angle $\varnothing \cong 82.87°$ across the sheet. This profile gives $B_{2\times0} = 1.5B_0$ and $B_{1\times0} = 0.5B_0$ where the subscripts "1" and "2" correspond to the magnetosheath and magnetosphere sides, respectively. The initial current sheet has a half thickness $L = 0.8d$, and it is shifted from $z = 0$ to $z = 3d_i$, to accommodate the larger structure expected in the weaker field side; the opening angle of the reconnection exhaust boundary on this side should be larger (Liu et al., 2018). The plasma has a density profile $n = n_0[1 - (S + S^2)/3]$ that gives $n_2 = n_0/3$ and $n_1 = n_0$. The uniform total temperature is $T = 3B_0^2/(8\pi n_0)$ that consists of contributions from ions and electrons with ratio $T_i/T_e = 5$. The mass ratio is $m_i/m_e = 25$. The ratio of the electron plasma to gyrofrequency is $\omega_{pe}/\Omega_{ce} = 4$ where $\omega_{pe} \equiv (4\pi n_0 e^2/m_e)^{1/2}$ and $\Omega_{ce} \equiv eB_0/m_e c$. In the presentation, densities, time, velocities, spatial scales, magnetic fields, and electric fields are normalized to n_0, the ion gyrofrequency Ω_{ci}, the Alfvénic speed $V_A \equiv B_0/(4\pi n_0 m_i)^{1/2}$, the ion inertia length $d_i \equiv c/\omega_{pi}$, B_0 and $V_A B_0/C$, respectively.

The x line orientation will be quantified by the angle θ respect to the y_0 axis illustrated in Figure 1. A clockwise rotation gives a negative θ. We can rotate the simulation box along the z axis by θ_{box} so that $\hat{\mathbf{x}} = \cos\theta_{box}\hat{\mathbf{x}}_0 - \sin\theta_{box}\hat{\mathbf{y}}_0$ and $\hat{\mathbf{y}} = \sin\theta_{box}\hat{\mathbf{x}}_0 + \cos\theta_{box}\hat{\mathbf{y}}_0$. The resulting magnetic field in the new coordinate will be

$$B_x(z) = B_{x0}(z)\cos\theta_{box} + B_{y0}\sin\theta_{box}, \qquad (1)$$
$$B_y(z) = -B_{x0}(z)\sin\theta_{box} + B_{y0}\cos\theta_{box}.$$

In a 2-D system, the orientation of the x line is fixed in the out-of-plane direction. This machinery allows us to study reconnection at a given x line orientation $\theta = \theta_{box}$.

The primary 3-D case has $\theta_{box} = 0°$, and it has a domain size $L_x \times L_y \times L_z = 256d_i \times 256d_i \times 24d_i$, and $4,096 \times 4,096 \times 384$ cells. The boundary conditions are periodic both in the x and y directions, while in the z direction they are conducting for fields and reflecting for particles. We use 200 particles per cell. Adopting the methodology in Liu etal.(2015), we localize the perturbation in both the x and y directions to initiate reconnection.

Companion 2-D and 3-D simulations with a much shorter y extent $\left(L_y = 32d_i\right)$ at a few representative oblique angles θ_{box} are designed to compare and contrast with the primary 3-D case.

3. X Line Orientation

Magnetic reconnection is initiated at the center of the simulation domain. The reconnection x line forms and spreads. In a slab geometry, a reconnection x line is best defined by the line of vanishing B_z, which is sandwiched between newly generated reconnected field B_z. The peak current density also serves as a good proxy to study the x line orientation when the x line is quasi-2-D (Liu et al., 2015). The total current density $|\mathbf{J}|$ at $y = 0$ and time $184/\Omega_{\text{ci}}$ is shown in Figure 2a. To study the orientation of this x line, we then take the x-y cut of a few quantities across the location of the intense current at $z/d_i \simeq 3.5$. The current density in

Figure 2b captures the distinct x line that is microscopically narrow but macroscopically long on the x-y plane. A movie that shows the evolution of $|\mathbf{J}|$ can be found in the supporting information. The x line in this case is surprisingly laminar and quasi-2-D, unlike most 3-D simulations where turbulence impacts the current sheet. The large guide field has suppressed the drift-kink instability (Karimabadi et al., 2003). The mild variability of the x line occurs when the intense current spreads and merges with the current intensified by the background tearing modes at two ends of this primary x line. For reference, the orientations of the asymptotic magnetic fields on both sides are marked by the yellow dashed arrows. The field strength is proportional to the arrow length. A straight line at orientation $-13°$ is also plotted for comparison. This is the x line orientation previously determined by the simulation in a 4 $\times 4 \times 1.5$ smaller spatial domain (illustrated by the green dashed box at the upper right corner of Figure 2b) and 3 times shorter evolution time *(60/Q$_{ci}$)* (Liu et al., 2015). In conjunction with Liu et al. (2015), the comparison demonstrates that this well-defined x line sustains the same orientation for at least $(184 - 60)/\Omega_{\text{cl}} = 124/\Omega_{\text{cl}}$, and we do not expect this orientation to change in a larger simulation. While the x line extent in Liu et al. (2015) is $\simeq 20d_i$, the x line in this larger simulation spread to a spatial length $\simeq 200d_i$, suggesting that

the x line extent in this regime is purely limited by the system size and there is no intrinsic length limitation in the 3-D system. In a slab geometry, the reconnected magnetic field B_z normal to the current sheet most faithfully captures the x line because it marks the change of the field-line connectivity. The B_z reversal in Figure 2 shows a similar orientation. The Alfvenic flow reversals serve as the strong indicative evidence of magnetic reconnection in in situ observations (e.g., Burch et al., 2016). The locus of outflow reversal locations, as captured by V_{ex} and V_{ix} in Figures 2d and 2e, also suggests a similar orientation. Also, note that in Figure 2c the clear stripe structure of B_z arises from the dominant oblique tearing modes that spontaneously grow from the ambient current sheet. The associated plasmoids are observed in Figure 2a for $|\mathrm{x}| \gtrsim 75d$, outside of the outflow region of the primary reconnection x line. These stripes make a similar orientation at $-13°$, and this fact has an implication for the x line stability that will be discussed later.

4. Break of the Frozen-in Condition

The sharp spatial gradient adjacent to the electron-scale diffusion region makes the ambient plasmas nongyrotropic. Figure 3a shows the nongyrotropy calculation (Aunai, Hesse & Kuznetsova 2013)$D_{ng} \equiv 2\sqrt{\sum_{ij} N_{ij}^2}/\ Tr\ (\mathbf{P})$ where the nongyrotropy tensor $N = P - P_{eg}$ measures the difference between the full pressure tensor and its gyrotropic approximation. Here $\mathbf{P}_{eg} \equiv P_{e\perp}\mathbf{I} + (P_{e\parallel} - P_{e\perp})\hat{\mathbf{b}}\hat{\mathbf{b}}$ with $P_{e\parallel} \equiv \hat{\mathbf{b}} \cdot \mathbf{P}_e \cdot \hat{\mathbf{b}}$ being the electron pressure parallel to the local magnetic field and $P_{e\perp} \equiv [\ Tr\ (\mathbf{P}_e) - P_{e\parallel}]/2$ being the pressure perpendicular to the local magnetic field. The intense D_{ng} traces the diffusion region and the sharp outflow exhaust boundaries. To assess the break of the electron frozen-in condition, we analyze the composition of the nonideal electric field (along the vertical white dashed line) using the electron momentum equation (i.e., Ohm's law)

$$en_e(\mathbf{E} + \mathbf{V}_e \times \mathbf{B}/c) + \nabla \cdot \mathbf{P}_e + m_e\nabla \cdot (n_e\mathbf{V}_e\mathbf{V}_e) + m_e\frac{\partial}{\partial t}(n_e\mathbf{V}_e) = 0. \quad (2)$$

In order to beat the PIC noise in this calculation, it is customary to ensemble average quantities. Since the meaning of "anomalous dissipations" arising from an ensemble average (either in a given space extent; Che et al., 2011; Le et al., 2017; Price et al., 2016 or time duration; Le et al., 2017) remains unclear (Le et al., 2018), here we average the entire equation without further splitting the nonlinear terms into a product of averaged quantities. The ensemble-averaged quantities are marked by the angle bracket in Figure 3b. $\langle \mathbf{Q} \rangle \cdot \hat{\mathbf{b}}$ indicates that the entire quantity $\mathbf{Q}$ is time averaged using 1,000 frames within duration $1.7/\Omega_{ci}$, then it is dotted with the averaged unit magnetic vector $\hat{\mathbf{b}} \equiv \langle \mathbf{B} \rangle / \langle B \rangle$. This shows the (time-averaged) quantity in the (time-averaged) parallel direction.

The peak nonideal electric field $\mathbf{E} + \mathbf{V}_e \times \mathbf{B}/\mathscr{C}$ in the parallel direction is primarily supported by the pressure tensor $\nabla \cdot P_e$ (green), and it closely resembles that in the corresponding 2-D simulation (Hesse et al., 2016; Lu et al., 2013). To further identify the key contribution in the full pressure tensors, it is useful to evaluate the divergence of its gyrotropic approximation. A similar decomposition is also analyzed in the observations of Magnetospheric Multiscale (MMS) mission (Genestreti et al., 2018; Rager et al., 2018). Outside of the diffusion region, $\nabla \cdot P_{eg} \cdot \hat{b}$ (brown) is a good approximation of $\nabla \cdot \langle \mathbf{P}_e \rangle \cdot \hat{\mathbf{b}}$. The contribution from the gyrotropic approximation vanishes near the location of the peak nonideal electric field, indicating that the primary contribution to the pressure gradient comes from the nongyrotropy. This is consistent with the idea made by the D_{ng} measurement in Figure 3a. We can further decompose the gyrotropic pressure gradient into $\nabla \cdot P_{eg} \cdot \hat{\mathbf{b}} = \partial_\parallel P_{e\parallel} - (P_{e\parallel} - P_{e\perp})\partial_\parallel \ln \langle B \rangle$ where $\partial_\parallel \equiv \hat{\mathbf{b}} \cdot \nabla$. The simulation result suggests that the gyrotropic contribution can be approximated by $\nabla \cdot P_{eg} \cdot \hat{b} \approx \partial_\parallel P_{e\parallel}$. That is, the

parallel gradient of the parallel component of the pressure tensor (magenta diamonds). The validity of this approximation is also observed in previous 3-D simulations (Liu et al., 2013).

5. Companion 2-D Simulations and Theories

Unlike the 3-D system where the x line has sufficient freedom to choose an optimal orientation, in 2-D systems the orientation of the x line is always fixed to the out-of-plane direction because of the translational invariance along this direction. Taking advantage of this artifact, we can study the property of reconnection in a specified orientation. On different oblique planes, the strength of the in-plane magnetic field varies according to equation (1). The in-plane component of magnetic field reverses sign for $\theta_{box} \in [-56.3°, 26.6°]$, and reconnection could operate on any of these oblique planes. In Figure 4a, we show the evolution of reconnection rates on few oblique planes ranging from $\theta_{box} = -25°$ to 10°. These rates are measured by calculating the change of the in-plane magnetic flux in between the X and O points. The measurement suggests that the reconnection rate is maximized at the orientation around −13° (red curve in Figure 4a), consistent with the orientation manifested in the 3-D simulation. This comparison between 3-D and 2-D systems demonstrates that reconnection proceeds near the maximal reconnection rate. (As an aside, this tendency of maximizing the rate revealed in 3-D simulations echoes the hypothesis used to derive the normalized asymmetric reconnection rate 0.1 in recent work Liu et al., 2018.)

Prompted by this agreement, we now compare our results to the prediction from different rate models. Cassak and Shay (2007) derived an expression of reconnection rate based on conservation laws, $E_{rec} \propto (B_{x1}B_{x2})^{1/2}(B_{x1} + B_{x2})^{-1/2}(B_{x1}\rho_2 + B_{x2}\rho_1)^{-1/2}$. Later, Birn et al. (2010) included the effect of compression and enthalpy in the calculation. Hesse etal. (2013) proposed that the reconnection rate is proportional to the available magnetic energy based on the reconnecting component $E_{rec} \propto B_{x1}^2 B_{x2}^2$, which always leads to a maximal rate at the bisection angle. Recently, Liu etal. (2018) modeled the reconnection rate as a function of the opening angle made by the upstream magnetic field. A prediction is attained by maximizing the model rate under the geometrical constraint imposed at the magnetohydrodynamics scale. Finally, since the stripe made by the dominant oblique tearing modes (presumably the fastest growing tearing modes) appears to be parallel to the x line orientation (Figure 2c), we also derive the growth rate of collisionless oblique tearing modes in Appendix A. It is not too surprising to see the dominant tearing mode sharing an orientation similar to that of the x line at its nonlinear state, because a tearing mode is the linear stage of spontaneous reconnection. As demonstrated in the next section, the fastest growing oblique tearing becomes active when the x line is forced to be oriented at an angle different from the optimal orientation.

These predicted reconnection rates are plotted in Figure 4b as a function of the x line orientation θ. To facilitate the identification of the optimal angle, each curve is normalized to its maximum. For reference, $\theta = -13°$ (the x line orientation) and 0° (the y_0 axis) are marked by the vertical dashed lines. We also plot the peak reconnection rates measured in Figure 4a as magenta diamonds. The linear growth rates of oblique tearing modes are plotted

as a cyan dashed curve. The growth rate based on a thick current sheet maximizes at $\theta \simeq -8°$. However, secondary tearing modes often grow from the nonlinear current sheet of d_e scale thickness and the tearing-mode simulation in a d_e scale sheet (Liu etal., 2015) showed the dominant mode with an orientation close to $\theta \simeq -13°$. After accounting fora narrow sheet at d_e scale, a modified theory (also derived in Appendix A) is plotted as the orange dashed curve. Two of the closest predictions of the x line orientation for this case are provided by Hesse etal. (2013) at the bisection angle $\theta \simeq -14.87°$ and the maximum of the modified tearing growth rate at $\theta \simeq -13.8°$. To distinguish which model works better in general will require a thorough parametric study. Nevertheless, these predictions range from $\theta \sim -8°$ to $-25°$ and are clearly off the y_0 axis at $\theta = 0°$. The observed x line orientation falls within this predicted range.

6. Orientation Versus Stability—A Numerical Experiment

At Earth's magnetopause, the initial reconnection line could be preconditioned by the global geometry and external forcing when a relatively planar solar wind touches the bell-shaped magnetosphere at the dayside. The local tangent of such a reconnection line may not necessarily align with the optimal orientation favored by the local physics. It is thus interesting to explore the stability of reconnection in a 3-D system when the x line does not point to the optimal orientation. As mentioned earlier, when the L_y boundary is extremely short, the quasi-2-D system fixes the x line to the y direction and completely suppresses any mode that has a finite k_y. In the following numerical experiments, we make L_y short to fix the x line in the y direction but long enough to allow the development of oblique tearing modes, which can spontaneously lead to competing reconnecting modes at different orientations.

In order to fit one oblique tearing mode of wavelength A at orientation θ inside the simulation domain, it requires $L_y \geq \lambda/\sin\theta$ (see Appendix B), and this wavelength needs to satisfy $2\pi/\lambda \lesssim k_c = [(1/2 + b_o \tan\theta)^2 + 1]^{1/2}/L$ for the unstable condition of tearing modes (i.e., $\Delta' \gtrsim 0$ calculated in the Appendix A). For an oblique tearing mode to grow at the optimal orientation $\theta = -13°$ in the initial current sheet of $L=0.8d_i$, it requires $L_y \gtrsim 15.5d_i$. The fastest growing mode typically has a wave number around $k_c/2$, and this will require $L_y \gtrsim 31d_i$. Thus, we choose $L_y=32d_i$, that should provide sufficient room for the oblique tearing mode to grow at this optimal orientation if its growth is desired. This y extent is 8 times shorter than the primary 3-D case, as illustrated by the green dashed box marked in Figure 2c. In addition, we apply a perturbation that is uniform in the y direction to initiate the x line.

In the first case, we keep $\theta_{box} = 0$. The evolution of reconnection is shown in Figure 5. The color shows the electron velocity V_{ey}. The most pronounced feature is the turbulence in Figures 5c and 5d, which is absent in the large 3-D case (Figure 2). Here we explain what gives rise to this turbulence. First of all, note that the primary x line points more or less in the y direction as initiated by the perturbation and soon enforced by the periodic boundary condition in the y direction. However, secondary tearing modes emerge on top of the primary x line in Figures 5a and 5b. These tearing modes are oblique to the primary x line in

the y direction, as illustrated by the B_z structure on the x-y plane in Figures 8a and 8b. Not too surprisingly, this structure is parallel to the optimal orientation at $\theta = -13°$ as marked by the white dashed line. The system radiates secondary tearing modes to adjust the orientation, but this attempt is destined to fail because of the large-scale orientation enforced by the periodic y boundary. The fast-streaming electrons resonated by tearing modes form intense electric current, which needs to close itself since $\nabla \cdot \mathbf{J} \simeq \nabla \cdot \left(\nabla \times c^2 \mathbf{B}/4\pi \right) \simeq 0$ in the nonrel-ativistic limit. The intense current structure leaves one y boundary at an oblique angle will come back from the other side farther downstream, forming a tearing chain along the entire separatrix and constantly feeding complexity back to the periodic system. In contrast, the x line and separatrix are quiet in the primary 3-D case (Figure 2).

In the second case, we rotate the simulation box to $\theta_{box} = -13°$ so that the y axis is along the optimal x line orientation. The evolution is shown in Figure 6. A secondary tearing mode appears in Figure 6a and soon disappears in the outflow. This secondary tearing mode forms structure parallel to the y direction, as expected, and it is easier to be advected out coherently and be merged in the outflow. The reconnection x line is thus considerably less turbulent. Oblique modes of smaller spatial scale later develop along the separatrix further downstream (Figure 6c). These modes could be lower hybrid drift modes or weaker oblique tearing modes. They eventually spread out and reach the x line (Figure 6d), perhaps, due to the combination of the x and y periodic boundaries. In the third case shown in Figure 7, we rotate the simulation box to $\theta_{box} = -35°$. Secondary tearing modes emerge and linger around the x line. This case further confirms that the secondary tearing modes do emerge along the optimal x line orientation, as shown in Figures 8e and 8f. Note that since the primary outflow speed driven by the preselected x line only varies as a function of the x location, segments on an oblique structure at different x locations are thus advected in different speeds (before the entire structure enters the region of a uniform Alfvenic outflow). Thus, the tilt angle of the oblique structure can become larger further downstream.

In short, these numerical experiments suggest that when the primary x line is forced to point at an orientation not favored by the local physics, the system radiates oblique tearing modes to adjust itself. The resulting oblique structure makes reconnection difficult to regain a coherent quasi-2-D structure inside a small periodic box.

7. Summary and Discussion

We studied the x line orientation and its stability using PIC simulations, showing that the x line in a large 3-D system (i.e., a proxy of an open system) proceeds along the orientation that maximizes the reconnection rate. The resulting diffusion region is laminar and the nongyrotropic feature of the pressure tensor breaks the frozen-in condition. In contrast, when the x line is externally forced to misalign with this optimal orientation, secondary oblique tearing modes develop to adjust the orientation. Inside a small periodic system, the oblique structure can hardly be expelled and merged. The fast-streaming electrons resonated by tearing modes quickly spread over the entire system, constantly feeding complex structure back to the periodic system and leading to turbulence. Based on these numerical

experiments, we conclude that the reconnection x line needs not be as turbulent as observed in small periodic simulations.

At Earth's magnetopause, a global reconnection line that misaligns with the optimal orientation favored by the local physics is expected to radiate secondary oblique tearing modes. However, the relatively large system may provide a sufficient room for the x line to adjust its orientation and to resume its natural, quieter state. To accurately model this reaction would require more realistic initial conditions, boundary conditions, and global external drives that are not yet feasible in a full PIC simulation. One possibility is that a misaligned reconnection line will breakup into smaller segments, which each are ideally aligned. This could explain localized bursts of reconnection in connection with flux transfer events. Note that the turbulence driven by the lower hybrid drift instability (LHDI) was discussed in MMS observation (Ergun et al., 2016; Graham et al., 2017) and the associated event studies using 3-D PIC simulations (Le et al., 2017; Price et al., 2016). For the parameters studied in this case, the LHDI appears to be relatively weak at the x line as shown in Figure 2a or 3a. The effect of LHDI on the x line is not the focus in this work, but the potential boundary effect inside a small periodic system also deserves future investigation. Note that this work does not imply that the generation of secondary flux ropes is entirely excluded when the x line develops along the optimal orientation. For instance, flux ropes were observed in the vicinity of the x line during tail reconnection (Wang et al., 2015,2010). Instead, this work suggests that an x line is inclined to generate secondary tearing modes when it misaligns with the optimal orientation.

We emphasize that an important nature of magnetic reconnection is revealed in this 3-D simulation; the comparison between the observed orientation and companion 2-D simulations in Figure 4a shows that reconnection tends to proceed at or, at least, near the maximal reconnection rate. This fact can be crucial for the explanation of the fast rate value of order 0.1; a recent model (Liu et al., 2017,2018) suggests that the reconnection rate profile as a function of the opening angle made by the upstream magnetic field is relatively flat near this optimal state, and it has a value of order 0.1.

In summary, this study advances our understanding of the 3-D orientation and stability of the asymmetric reconnection x line. This result could help interpret the local geometry of reconnection events observed by MMS and, perhaps, help determine an appropriate LMN coordinate (Denton et al., 2018). The question we are exploring is also relevant to the upcoming European Space Agency-Chinese Academy of Sciences joint mission, Solar wind Magnetosphere Ionosphere Link Explorer, which will study the development of reconnection lines at Earth's magnetopause using X-ray and ultraviolet imagers.

Supplementary Material

Refer to Web version on PubMed Central for supplementary material.

Acknowledgments

Appendix A:

Collisionless Tearing Growth Rate

In addition to obtaining an optimal orientation by maximizing the reconnection rate, it is also interesting to consider the competition of linear tearing modes that lead to spontaneous reconnection.

We consider the collisionless tearing stability of this configuration for an arbitrary wavevector $\mathbf{k} = k_x\hat{\mathbf{x}} + k_y\hat{\mathbf{y}}$ corresponding to oblique angle $\theta \equiv \tan^{-1}\left(k_y/k_x\right)$ and resonance surface $z_s = -L \times arctanh \left(1/2 + b_g\tan\theta\right) + 3d_i$, at $F \equiv \mathbf{k} \cdot \mathbf{B} = 0$. In the outer region, the magnetohydrodynamic model is used to obtain an eigenmode equation (Furth et al., 1963) of the form $\Psi'' = \left(k^2 + F''/F\right)\widetilde{\Psi}$, where $\widetilde{\psi}(z)$ is the perturbed flux function at the oblique plane and $k^2 \equiv k_x^2 + k_y^2$. By combining the approximate solutions for $kL \ll 1$ and $kL \gg$ and $k^2 \equiv k_x^2 + k_y^2$ in the same manner as in Baalrud et al. (2012), we get the drive for tearing perturbations (Furth et al., 1963) $\Delta' \equiv \lim_{\epsilon \to 0}(1/\widetilde{\psi})[d\widetilde{\psi}/dz]_{z_5 - \epsilon}^{Z_s + \epsilon} \simeq \left(\alpha^2/k\right)\left(F_{-\infty}^{-2} + F_{\infty}^{-2}\right) - 2k$ where $\alpha \equiv (dF/dz)_{z = z_S}$. Plugging in our configuration, it gives

$$\Delta' \simeq \frac{2\left[\left(1/2 + b_g\tan\theta\right)^2 + 1\right]}{kL^2} - 2k. \quad \text{(A1)}$$

The upper bound of the unstable wave number is $k_cL \lesssim \left[(1/2 + b, \tan\theta)^2 + 1\right]^{1/2}$. Using the standard matching approach (Daughton et al., 2011; Drake & Lee, 1977) to the kinetic resonance layer gives

$$\gamma \simeq \frac{d_e^2\Delta'}{l_s}kv_{\text{the}}, \quad \text{(A2)}$$

where $v_{\text{the}} \equiv \left(2T_e/m_e\right)^{1/2}$ is the electron thermal speed and $d_e = c/w_{pe}$ is the local electron inertial length at the resonant surface. l_s is the scale length of the magnetic shear defined in $k_{\parallel} = \mathbf{k} \cdot \mathbf{B}/\left|\mathbf{B}\right| \approx [\partial(\mathbf{k}\mathbf{B}/|\mathbf{B}|)/\partial z]_{z = z_s}\left(z - z_s\right) \equiv k(z - z_s)/l_s$. It is derived to be

$$l_s = \frac{Lb_g\left(1 + \tan^2\theta\right)^{1/2}}{\left[1 - \left(1/2 + b_g\tan\theta\right)^2\right]\cos\theta}.$$

The dominant mode typically has a wavelength $kL \sim k_c L/2$, and it is roughly 0.5. Based on this wave number ($k_c/2$), the growth rate at the different oblique angle is shown by the dashed cyan curve in Figure 4b, which has a maximum at $\theta \simeq -8°$.

The width of the resonant surface A is determined by the resonant condition (Drake & Lee, 1977) $\gamma \simeq k_\parallel V_{the} = \left(k\Delta/l_s\right)v_{the}$ and it should be limited by the thickness of the current sheet L. Thus, by comparing with equation (A2) we can derive $\Delta'd_e \simeq \Delta/d_e \leq L/d_e$. For $L/d_e \leq 1$, we have $\Delta'd_e \leq 1$. On the other hand, equation (A1) with $k \simeq k_c/2$ suggests $\Delta'd_e \simeq 1/\left(L/d_e\right) \geq 1$ in the same limit. It is thus clear that the theory breaks down for a narrow sheet $L/d_e < 1$. As a quick remedy, we argue $\Delta'd_e \simeq 1$, and thus, $\gamma \simeq d_e k v_{the}/l_s$. This modified rate for a d_e scale sheet is plotted as the orange dashed curve in Figure 4b, which has a maximum at $\theta \simeq -13.8°$, comparable to the oblique angle ($\simeq -13°$) of the dominant mode observed in a d_e scale sheet (Liu et al., 2015).

Appendix B:

The Minimum Box Size Required for an Oblique Mode

To perfectly fit an oblique mode of angle θ and wavelength X inside a box of periodic y boundary, as shown in Figure B1, it requires $L_y = N\lambda/\sin\theta$ where N is a positive integer. For $L_y < \lambda/\sin\theta$, the mode can at least partially manifest its orientation. For $L_y < \lambda/\sin\theta$, such a mode is impossible to grow due to the effect of the periodic boundary.
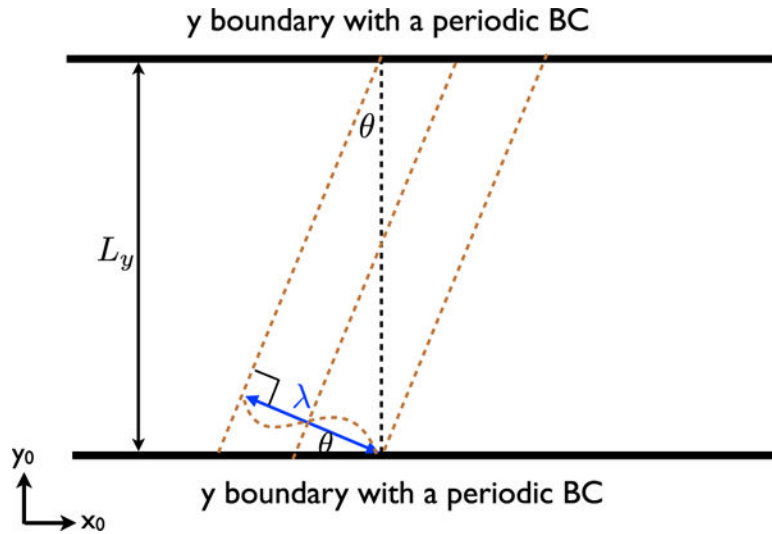

Figure B1.

The system size Ly that perfectly fit an oblique mode of angle θ and wavelength λ.

References

Alexeev II, Sibeck DG, & Bobrovnikov SY (1998). Concerning the location of magnetopause merging as a function of the magnetopause current sheet. Journal ofGeophysical Research, 103(A4), 6675–6684.

Aunai N, Hesse M, & Kuznetsova M (2013). Electron nongyrotropy in the context of collisionless magnetic reconnection. Physics of P/asmas, 20,92903.

Aunai N, Hesse M, Lavraud B, Dargent J, & Smets R (2016). Orientation of thex-line in asymmetric magnetic reconnection. Journal of Plasma Physics, 82,535820401.

Aunai N, Hesse M, Zenitani S, Kuznetsova M, Black C, Evans R, & Smets R (2013). Comparison between hybrid and fully kinetic models of asymmetric magnetic reconnection: Coplanar and guide field configuration. Physics of Plasmas, 20, 22902.

Baalrud SD, Bhattacharjee A, & Huang YM (2012). Reduced magnetohydrodynamic theory of oblique plasmoid instabilities. Physics of P/asmas, 19,22101.

Birn J, Borovsky JE, Hesse M, & Schindler K (2010). Scaling of asymmetric reconnection in compressible plasmas. Physics of Plasmas, 17, 52108.

Bowers K, Albright B, Yin L, Daughton W, Roytershteyn V, Bergen B, & Kwan T (2009). Advances in petascale kinetic simulation with VPIC and Roadrunner. Journal ofPhysics: Conference Series, 180,12055.

Burch JL, Tobert RB, Phan T, Chen LJ, Moore TE, Ergun RE, et al. (2016). Electron-scale measurements of magnetic reconnection in space. Science, 352, aaf2939. [PubMed: 27174677]

Cassak PA, & Shay MA (2007). Scaling of asymmetric magnetic reconnection: General theory and collisional simulations. Physics of P/asmas, 14,102114.

Che H, Drake JF, &Swisdak M (2011). A current filamentation mechanism for breaking magnetic field lines during reconnection. Nature, 474(7350), 184–187. 10.1038/nature10091 [PubMed: 21633355]

Cowley SWH (1973). A quanlitative study of the reconnection between the earth's magnetic field and an interplanetary field of arbitrary orientation. Radio Science, 8(11), 903–913.

Daly PW, Saunders MA, Rijnbeek RP, Sckopke N, & Russell CT (1984). The distribution of reconnection geometry in flux transfer events using energetic ion, plasma and magnetic data. Journal of GeophysicalResearch, 89(A6), 3843–3854.

Daughton W, Roytershteyn V, Karimabadi H, Yin L, Albright BJ, Bergen B, & Bowers KJ (2011). Role of electron physics in the development of turbulent magnetic reconnection in collisionless plasmas. Nature Physics, 7, 539–542. 10.1038/nphys1965

Denton RE, Sonnerup BUO, Russell CT, Hasegawa H, Phan T-D, Strangeway RJ, et al. (2018). Determining L-M-N current sheet coordinate at the magnetopause from Magnetospheric Multiscale data. Journal ofGeophysical Research: Space Physics, 123, 2274–2295. 10.1002/2017JA024619

Dorelli JC, Bhattacharjee A, & Raeder J (2007). Separator reconnection at Earth's dayside magnetopause under generic northward interplanetary magnetic field conditions. Journal ofGeophysical Research, 112, A02202 10.1029/2006JA011877

Drake JF, & Lee YC (1977). Nonlinear evolution of collisionless and semicollisional tearing modes. Physics of Fluids, 20(8), 1341–1353.

Dungey J (1961). Interplanetary magnetic field and the auroral zones. Physical ReviewLetters, 6(2), 47–48.

Dunlop MW, Zhang QH, Bogdanova YV, Lockwood M, Pu Z, Hasegawa H, et al. (2011). Extented magnetic reconnection across the dayside magnetopause. Physical Review Letters, 107,025004. [PubMed: 21797615]

Dunlop MW, Zhang QH, Bogdanova YV, Trattner KJ, Pu Z, Hasegawa H, et al. (2011). Magnetopause reconnection across wide local time. Annales de Geophysique, 29,1683–1697.

Ergun RE, Goodrich KA, Wilder FD, Holmes JC, Stawarz JE, Eriksson S, et al. (2016). Magnetospheric multiscale satellites observations of parallel electric fields associated with magnetic reconnection. Physical ReviewLetters, 116,235102.

Fear RC, Palmroth M, & Milan SE (2012). Seasonal and clock angle control of the location of flux transfer event signatures at the magnetopause. Journal ofGeophysical Research, 117, A04202 10.1029/2011JA017235

Furth H, Killeen J, & Rosenbluth MN (1963). Finite-resistivity instability of sheet pinch. Physics ofFluids, 6,459–484.

Genestreti KJ, Varsani A, Burch JL, Cassak PA, Torbert RB, Nakamura R, et al. (2018). MMS observation of asymmetric reconnection supportedby3-Delectronpressuredivergence.GeophysicalResearchLetters,123,1806–1821.10.1002/2017JA025019

Gonzalez WD, & Mozer FS (1974). A quantitative model for the potential resulting from reconnection with an arbitrary interplanetary magnetic field. Journal ofGeophysical Research, 79(28), 4186–4194.

Graham DB, Khotyaintsev YV, Norgren C, Vaivads A, André M, Toledo-Rendondo S, et al. (2017). Lower hybrid waves in the ion diffusion and magnetospheric inflow regions. Journal of Geophysical Research: Space Physics, 122, 517–533. 10.1002/2016JA023572

Hesse M, Aunai N, Zenitani S, Kuznetsova M, & Birn J (2013). Aspects of collisionless magnetic reconnection in asymmetric systems. Physics of Plasmas, 20,61210.

Hesse M, Liu Y, Chen L-J, Bessho N, Kuznetsova M, Birn J, & Burch JL (2016). On the electron diffusion region in asymmetric reconnection with a guide magnetic field. Geophysical Research Letters, 43,2359–2364. 10.1002/2016GL068373

Karimabadi H, Daughton W, Pritchett PL, & Krauss-Varban D (2003). Ion-ion kink instability in the magnetotail: 1. Linear theory. Journal ofGeophysicalResearch, 108(A11), 1400 10.1029/2003JA010026

Kawano H, & Russell CT (2005). Dual-satellite observations of the motions of flux transfer events: Statistical analysis with ISEE 1 and ISEE 2. Journal ofGeophysical Research, 110, A07217 10.1029/2004JA010821

Komar CM, Cassak PA, Dorelli JC, Glocer A, & Kuznetsova MM (2013). Tracing magnetic separators and their dependence on IMF clock angle in global magnetospheric simulations. Journal of Geophysical Research: Space Physics, 118, 4998–5007. 10.1002/jgra.50479

Komar CM, Fermo RL, & Cassak PA (2015). Comparative analysis of dayside magnetic reconnection models in global magnetosphere simulations. Journal ofGeophysical Research: Space Physics, 120, 276–294. 10.1002/2014JA020587

Le A, Daughton W, Chen L-J, & Egedal J (2017). Enhanced electron mixing and heating in 3-D asymmetric reconnection at the Earth's magnetopause. Geophysical Research Letters, 44,2096–2104. 10.1002/2017GL072522

Le A, Daughton W, Ohia O, Chen LJ, & Liu Y-H (2018). Drift turbulence, particle transport, and anomalous dissipation at the reconnection magnetopause. arXiv:xxxx.

Liu Y-H, Daughton W, Karimabadi H, Li H, & Roytershteyn V (2013). Bifurcated structure of the electron diffusion region in three-dimensional magnetic reconnection. PhysicalReviewLetters, 110(265004).

Liu Y-H, Hesse M, Cassak PA, Shay MA, Wang S, &Chen L-J (2018). On the collisionless asymmetric magnetic reconnection rate. Geophysical Research Letters, 45,3311–3318. 10.1002/2017GL076460 [PubMed: 30245534]

Liu Y-H, Hesse M, Guo F, Daughton W, Li H, Cassak PA, & Shay MA (2017). Why does steady-state magnetic reconnection have a maximum local rate of order 0.1? Physical Review Letters, 118,85101.

Liu Y-H, Hesse M, & Kuznetsova M (2015). Orientation of x lines in asymmetric magnetic reconnection — Mass ratio dependency. Journal ofGeophysical Research: Space Physics, 120, 7331–7341. 10.1002/2015JA021324

Lu Q, Lu S, Huang C, Wu M, & Wang S (2013). Self-reinforcing process of the reconnection electric field in the electron diffusion region and onset of collisionless magnetic reconnection. PlasmaPhysics and Controlled Fusion, 55, 85019.

Papadopoulos K, Goodrich C, Wiltberger M, Lopez R, & Lyon J (1999). The physics of substorms as revealed by the ISTP. Physics and Chemistry of the Earth, Part C, 24,189–202.

Phan TD, Gosling JT, Davis MS, Skoug RM, Øieroset M, Lin RP, et al. (2006). A magnetic reconnection X-line extending more than 390 Earth radii in the solar wind. Nature, 439,175–178. 10.1038/nature04393 [PubMed: 16407946]

Price L, Swisdak M, Drake JF, Cassak PA, Dahlin JT, & Ergun RE (2016). The effects of turbulence on three-dimensional magnetic reconnection at the magnetopause. Geophysical Research Letters, 43,6020–6027. 10.1002/2016GL069578

Pritchett PL (2008). Collisionless magnetic reconnection in an asymmetric current sheet. JournalofGeophysical Research, 113, A0621010.1029/2007JA012930

Pu ZY, Zhang XG, Wang XG, Wang J, Zhou XZ, Dunlop MW, et al. (2007). Global view of dayside magnetic reconnection with the dusk-dawn IMF orientation: A statistical study for Double Star and Cluster data. Geophysical Research Letters, 34, L20101 10.1029/2007GL030336

Rager AC, Dorelli JC, Gershman DJ, Uritsky V, Avanov LA, Torbert RB, et al. (2018). Electron crescent distributions as a manifestation of diamagnetic drift in an electron-scale current sheet: Magnetospheric multiscale observations using new 7.5 ms fast plasma investigation moments. Geophysical Research Letters, 45,578–584. 10.1002/2017GL076260 [PubMed: 29576666]

Schreier R, Swisdak M, Drake JF, & Cassak PA (2010). Three-dimensional simulations of the orientation and structure of reconnection x-lines. Physics ofPlasmas, 17(110704).

Scurry L, Russell CT, & Gosling JT (1994). A statistical study of accelerated flow events at the dayside magnetopause. Journal of Geophysical Research, 99(A8), 14,815–14,829.

Siscoe GL, Erickson GM, Sonnerup BUÖ, Maynard NC, Siebert KD, Weimer DR, & White WW (2001). Global role of ey in magnetopausereconnection:Anexplicitdemonstration.JournalofGeophysicalResearch,106,13,015–13,022.

Sonnerup BUÖ (1974). Magnetopause reconnection rate. JournalofGeophysicalResearch, 79(10), 1546–1549.

Swisdak M, & Drake JF (2007). Orientation of the reconnection x-line. Geophysical Research Letters, 34, L11106 10.1029/2007GL029815

Trattner KJ, Fuselier SA, & Petrinec SM (2004). Location of the reconnection line for northward interplanetary magnetic field. Journal ofGeophysical Research, 109, A03219 10.1029/2003JA009975

Trattner KJ, Mulcock JS, Petrinec SM, & Fuselier SA (2007). Probing the boundary between antiparallel and component reconnection during southward interplanetary magneitc field conditions. Journal of Geophysical Research, 112, A01201 10.1029/2007JA012270

Wang R, Lu Q, Du A, & Wang S (2010). In situ observations of a secondary magnetic island in an ion diffusion region and associated energetic electrons. Physical Review Letters, 104(175003).

Wang R, Lu Q, Nakamura R, Huang C, Du A, Guo F, et al. (2015). Coalescence of magnetic flux ropes in the ion diffusion region of magneticreconnection.NaturePhysics,12,263–267.

Wild JA, Milan SE, Davies JA, Dunlop MW, Wright DM, Carr CM, et al. (2007). On the location of dayside magnetic reconnection during an interval of duskward oriented IMF. Annales de Geophysique, 25, 219–238.

Key Points:

- The orientation of asymmetric reconnection x line is studied using large 3-D particle-in-cell simulations

- Companion 2-D simulations indicate that the 3-D system selects a state of, or at least near, the maximal reconnection rate

- The system tends to radiates secondary oblique tearing modes when the primary x line is forced to misalign with this optimal orientation
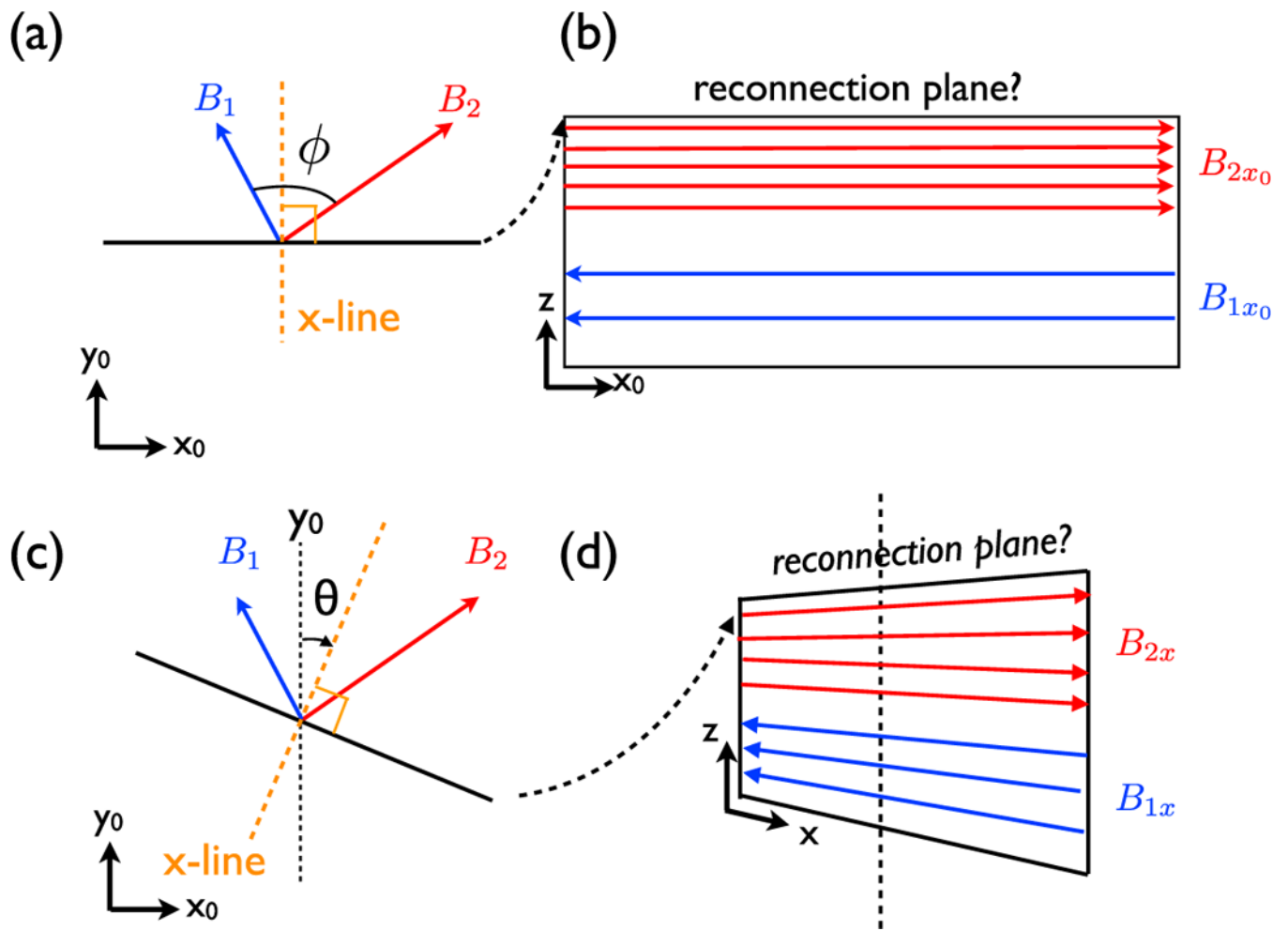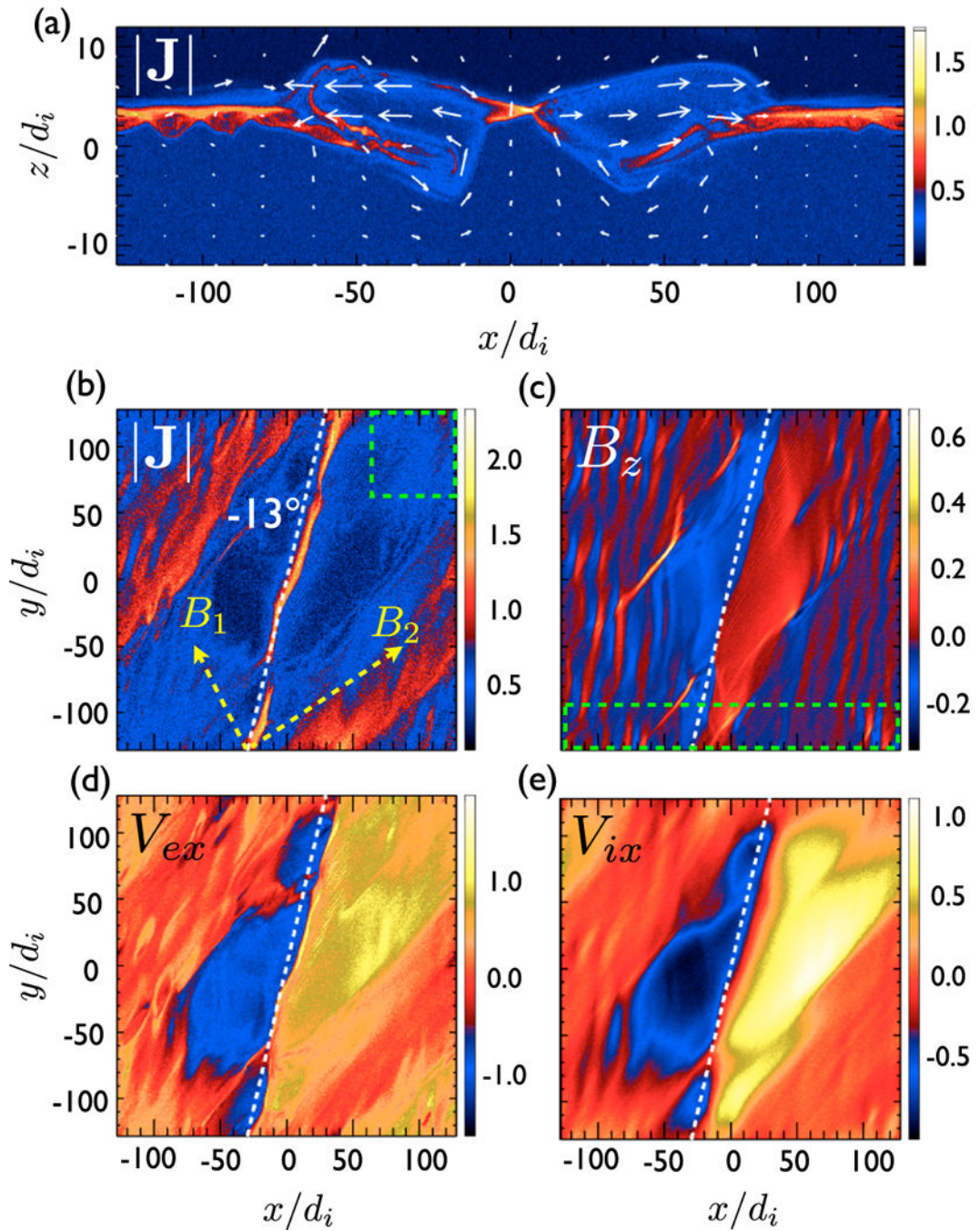
Figure 1.
Illustration of the question to solve.

Figure 2.
Quantities at time $184/\Omega_{ci}$. In (a) the total current density $|\mathbf{J}|$ on a 2-D plane where $y = 0$. The white arrows show the in-plane electron velocities. In (b) the x-y cut of $|\mathbf{J}|$ across the location of the intense current near the x line. Similarly, in (c), the reconnected field B_z; in (d), the electron outflow V_{ex}; and in (e), the ion outflow V_{ix}. On top of the figures, yellow arrowed lines in (b) illustrate the magnetic fields on two sides of the current sheet, and white dashed lines in (b)-(e) have $\vartheta = -13°$.
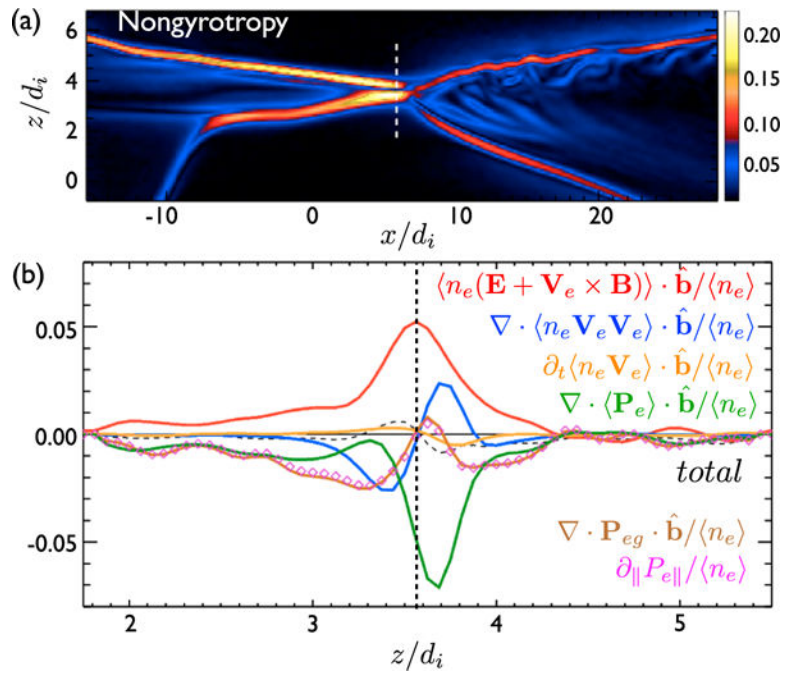
Figure 3.

In (a) the measure of the nongyrotropy (D_{ng}) of the pressure tensor. In (b) the decomposition of the nonideal electric field. The charge e and electron mass m_e are normalized to unity in our presentation.
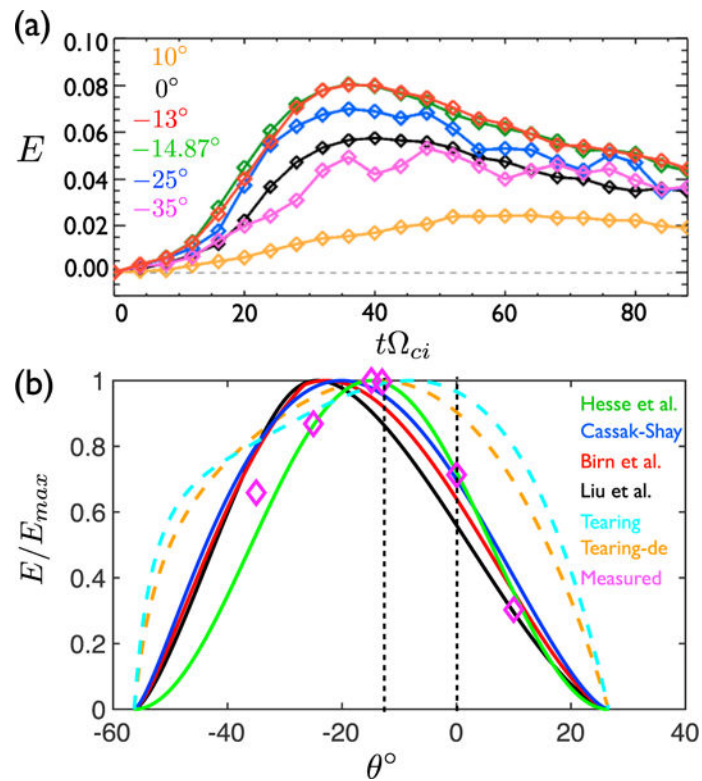
Figure 4.

In (a) the evolution of the reconnection rate (E) measured on a sample of oblique planes at different θ_{box}. In (b), "Hesse et al.," "Cassak-Shay," "Birn et al.," and "Liu et al." are the predicted reconnection rates from different models. "Tearing" shows the tearing growth rate derived in Appendix A and "Tearing-de" is the modified growth rate in a d_e scale sheet. The measured rates from (a) are plotted as magenta diamonds. Each curve is normalized to its maximum value.
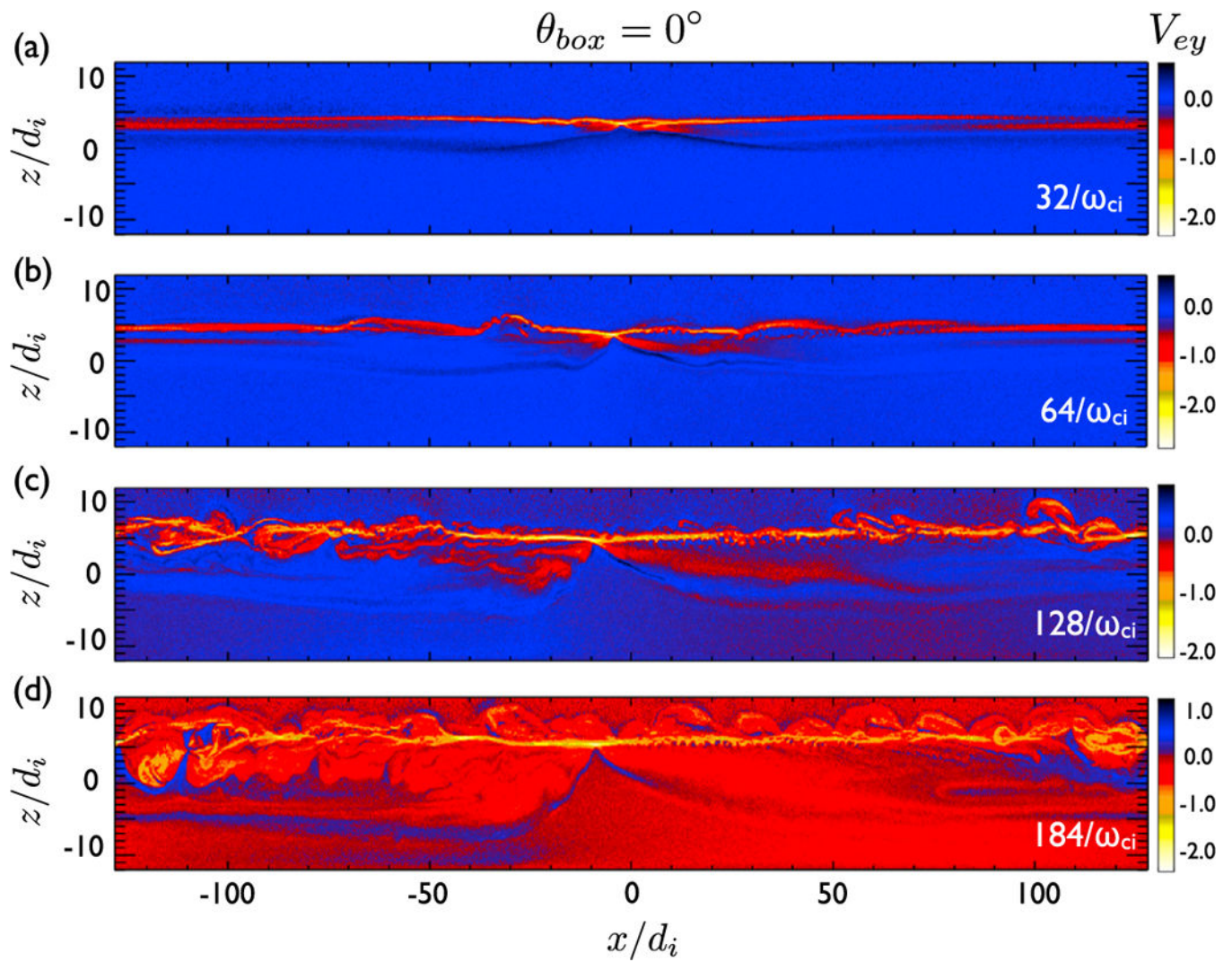
Figure 5.
The evolution of reconnection in a companion 3-D simulation using $L_y = 32 d_i$, and $\theta_{box} = 0°$. The color shows the electron flow speed in the y direction (V_{ey}).
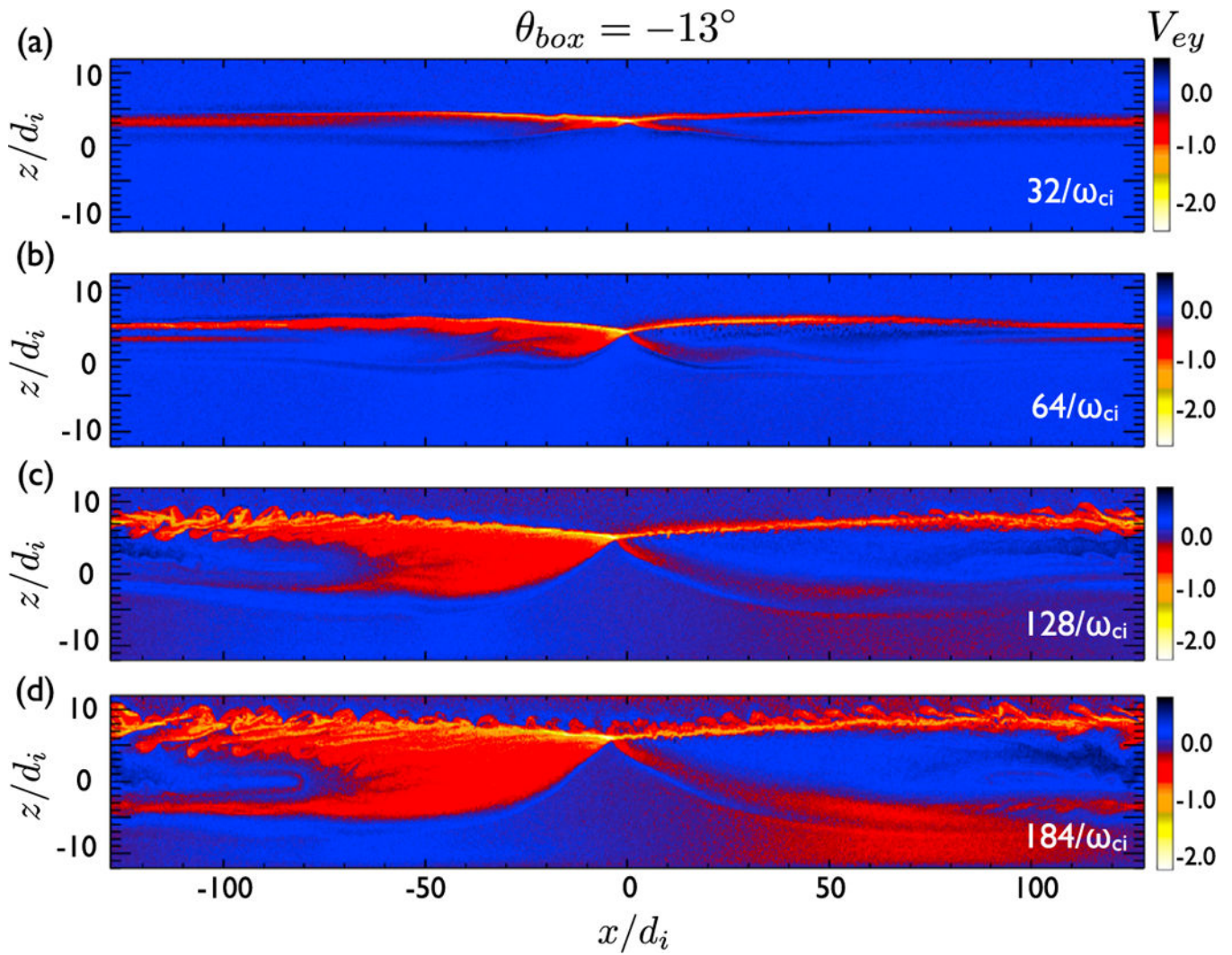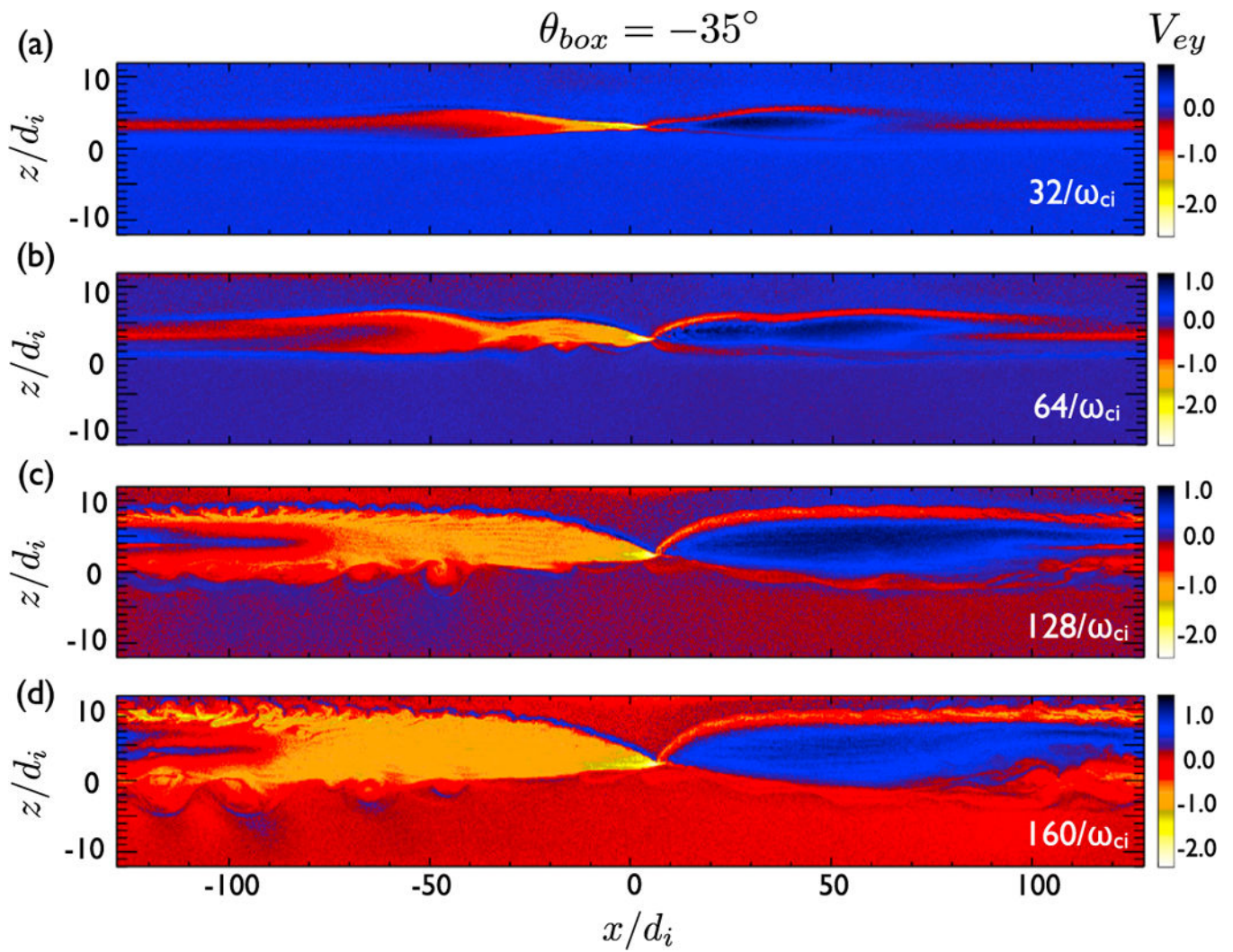
Figure 6.
The evolution of reconnection in a companion 3-D*i* simulation using $Ly = 32d$, and $\theta_{box} = -13°$. The color shows the electron flow speed in the y direction (V_{ey}).

Figure 7.
The evolution of reconnection in a companion 3-D simulation using $Ly = 32di$, and $\theta_{box} = -35°$. The color shows the electron flow speed in the y direction (V_{ey}).
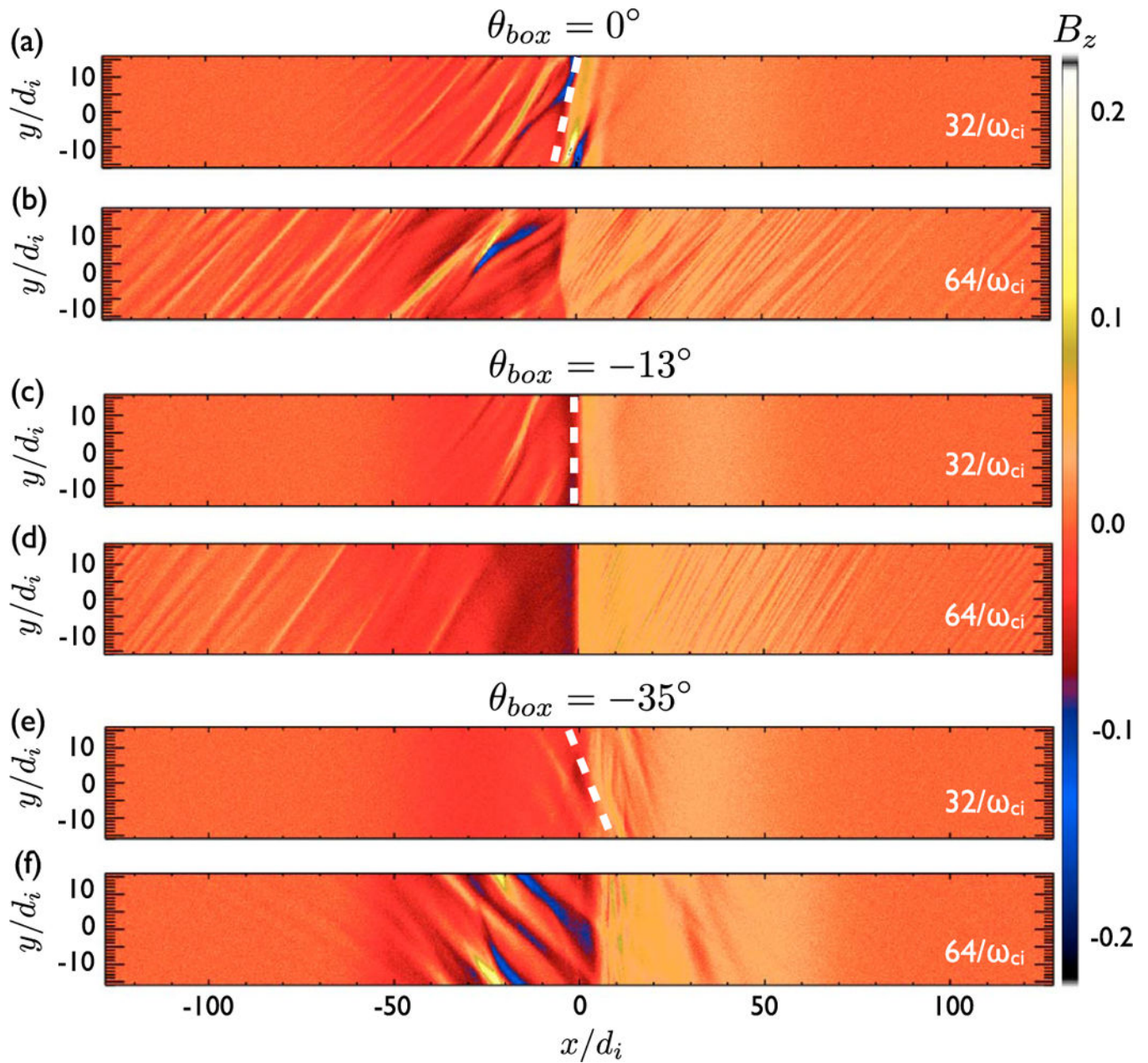
Figure 8.
The B_z structure in the x-y plane that contain the x line in companion 3-D simulation using $Ly = 32di$. In (a) and (b) $\theta_{box} = 0°$, in (c) and (d) $\theta_{box} = -13°$, and in (e) and (f) $\theta_{box} = -35°$. The white dashed lines mark the orientation ($\theta = -13°$) favored by the local physics.